Check for updates

Received: 14 January 2021 | Revised: 30 April 2021 | Accepted: 30 April 2021

DOI: 10.1111/ffe.13493

ORIGINAL ARTICLE

FFEMS Fatigue & Fracture of Engineering Materials & Structures WILEY

Crack tip microplasticity mediated by microstructure gradients

Gustavo M. Castelluccio[1] | Hojun Lim[2] | John M. Emery[2] | Corbett C. Battaile[2]

[1]School of Aerospace, Transport and Manufacturing, Cranfield University, Bedford, MK43 0AL, UK

[2]Department of Computational Materials and Data Science, Sandia National Laboratories, Albuquerque, New Mexico, NM 87185, USA

Correspondence
Gustavo Castelluccio, Cranfield University, Cranfield, Bedfordshire, MK43 0AL, UK,
Email: castellg@cranfield.ac.uk

Funding information
Sandia National Laboratories, Grant/Award Number: Exploratory Express LDRD project 193072

Abstract

Traditional fracture theories infer damage at cracks (local field) by surveying loading conditions away from cracks (far field). This approach has been successful in predicting ductile fracture, but it normally assumes isotropic and homogeneous materials. However, myriads of manufacturing procedures induce heterogeneous microstructural gradients that can affect the accuracy of traditional fracture models. This work presents a microstructure-sensitive finite element approach to explore the shielding effects of grain size and crystallographic orientation gradients on crack tip microplasticity and blunting. A dislocation density-based crystal plasticity model conveys texture evolution, grain size effects, and directional hardening by computing the constraint from dislocation structures. The results demonstrate that the microstructure can act as a buffer between the local and far fields that affects the crack tip microplasticity variability. For nominal opening loading, grain size and texture affect the local ductility and induce a non-negligible multiaxial plastic deformation. Furthermore, driving forces based on measuring displacements away from the crack tip are less affected by the microstructure, which suggests that traditional experimental methods smear out important crack tip variability.

KEYWORDS

crack tip displacement, crystal plasticity, grain size, microplasticity, microstructure

1 | INTRODUCTION

Ductile failure in metals is an intrinsic multiscale problem: forces applied far from a crack translate into crack blunting, growth, and failure, which are controlled by atom decohesion and defect aggregation (e.g., dislocations and vacancies). In between, microstructural attributes such as grain morphology, lattice orientation, material phases, and heterogeneous defect densities regulate the fracture driving force at the crack tip. As a result, fracture mechanics driving forces—e.g., crack tip opening displacement (CTOD), stress intensity factor (K), and J-integral[1]—depend on the microstructure in between the local and the far field.

Traditional fracture approaches assume homogeneous and isotropic materials with self-similar crack tip stress and strain fields,[2] which may not be representative of heterogeneous materials. Indeed, the J-integral becomes path-dependent[3,4] for a crack growing towards an interface (Figure 1) with different material properties (e.g., welded material or a grain boundary). The J-integral in the neighborhood of the crack tip (J_{tip})[5] may still

This is an open access article under the terms of the Creative Commons Attribution License, which permits use, distribution and reproduction in any medium, provided the original work is properly cited.
© 2021 The Authors. *Fatigue & Fracture of Engineering Materials & Structures* published by John Wiley & Sons Ltd. This article has been contributed to by US Government employees and their work is in the public domain in the USA.

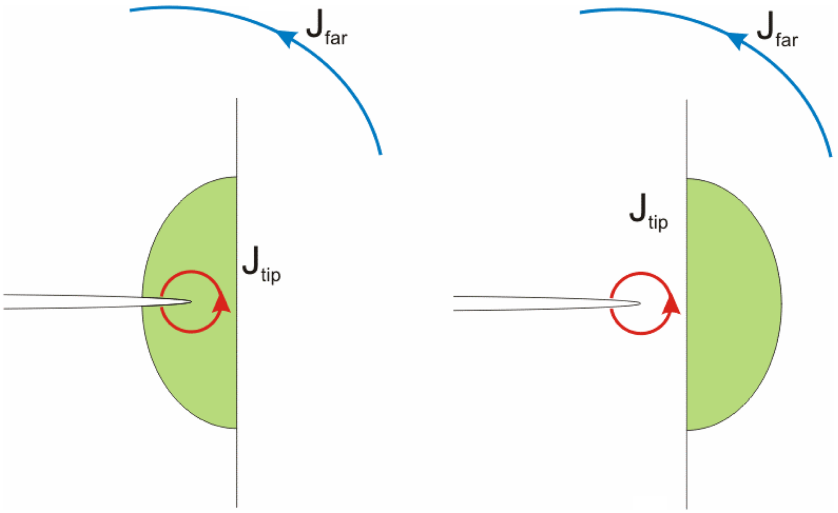


FIGURE 1 Crack-tip shielding or amplification of plastic zones that are indicated by the shaded areas. (left) crack-tip shielding $J_{tip} < J_{far}$; (right) crack-tip amplification $J_{tip} > J_{far}$ [Colour figure can be viewed at wileyonlinelibrary.com]

represent the crack growth driving force, but its value differs from the J-integral measured far from the crack (J_{far}). In consequence, standardized K and J-integral (e.g., ASTM E1820[6] and BS 7448[7]) may not yield accurate predictions of the driving force that controls the fracture process.

The decisive role of the microstructure on fracture has been extensively demonstrated experimentally, and it is well established in the literature.[8,9] For example, fracture toughness in metals with moderate ductility often increases upon grain size refinement.[10–12] However, fracture mechanics theories cannot predict the role of the microstructure on fracture driving forces,[13] and they rely on microstructure-sensitive coefficients that are calibrated empirically. This approach results in limited physical understanding and large epistemic uncertainty.[14,15]

Physics-based computational models can contribute to fracture theories[16] with predictive approaches that identify toughening mechanisms at the micro- and meso-scales.[17–19] Recent research[20–24] quantified the role of microstructure on fatigue and fracture by integrating multiscale physics-based modeling. Other researchers[25,26] employed continuum models to engineer crack paths by controlling the distribution of second phases. Parallel efforts explored the anomalous fracture of nanocrystals by theorizing various toughening mechanisms.[23,27,28] However, limited work has focuses on understanding the effects of microstructure gradients on crack tip deformation, even when these gradients are common in manufacturing processes (e.g., welding, electrodeposition, and additive manufacturing).

This work employs microstructure-sensitive finite element models to quantify the effects of microstructural gradients on crack tip microplasticity and blunting. We adopt a physics-based crystal plasticity model for FCC metals that explicitly represents the grain morphology and crystallographic texture for stationary cracks with different microstructural gradients. The comparison of displacement-based fracture driving forces (e.g., CTOD) provides a simple and unambiguous basis for evaluating microstructures that can mitigate the onset of ductile fracture.

2 | FINITE ELEMENT MODELING

We employ a crystal plasticity formulation to quantify the effects of microstucture on crack tip deformation prior to crack growth. We focus on understanding the transition from elastic to incipient plastic blunting, but prior to profuse void growth and coalescence (e.g., maximum plastic strain in any element is less than 10%). Such a regime is marked by anisotropic plastic deformation and strong sensitivity to microstructure, which precondition the final fracture failure (being either fully ductile or quasi-brittle).

2.1 | Constitutive model

Crystal plasticity formulations[29,30] are among the simplest continuum models that quantify plastic anisotropy, and they have advanced substantially in the last decades.[31,32] Heterogeneous grain-level deformation is extremely difficult to describe with higher length scale models such as isotropic J_2 plasticity theory. Other approaches have described microstructure size effects in plastic deformation by means of homogenized phenomenological strain gradient theories,[33,34] but neither this nor J_2 theories track slip system activity or its crystallographic orientation dependence.

Recent advances in crystal plasticity have formulated physics-based approaches that describe deformation

mechanisms at multiple scales.[35] For example, the understanding of atomistic-scale response has informed phenomenological parametrizations[36] of dislocation glide activation[37–39] or dislocation-dislocation interactions.[40,41] However, bottom-up approaches fall short in representing dislocation patterning and heterogeneous deformation, which have a strong effect on the mechanical response.[42–45] Some efforts have informed continuum with mesoscale dislocation structures from dislocation dynamics models,[46,47] but their applicability is usually limited to specific crystal orientations, reduced domain size, and small plastic strains.

Castelluccio and McDowell[48] proposed a crystal plasticity approach that describes commonalities of dislocation structures following transmission electron microscopy and the similitude principle.[49,50] This model, which was originally proposed and calibrated for cyclic deformation of nickel, is extended here to monotonic loading. The calculations are implemented as an Abaqus user subroutine (UMAT)[51] and convey the physics of dislocation interactions at multiple length scales. The formulation and parameters are identical to those presented earlier,[48] except for the evolution of the dislocation structures, which are assumed to be cells from the beginning.

At the atomic scale unit process, the shear rate of the α-th slip system follows the approach proposed by Busso,[52] which relies on the Arrhenius thermal activation formulation by Kocks et al.[36,53]

$$\dot{\gamma}^{\alpha}=\rho_m^{\alpha} l_{struct} b \nu_G \exp\left(-\frac{F_0}{k_b T}\left\langle 1-\left[\frac{\left\langle\left|\tau_{eff}^{\alpha}\right|-S^{\alpha}\right\rangle}{s_t^0 \frac{C_{44}}{C_{44}^0}}\right]^{p}\right\rangle^{q}\right)\operatorname{sgn}\left(\tau_{eff}^{\alpha}\right). \tag{1}$$

Here, $\langle\ \rangle$ corresponds to the Macaulay brackets, ρ_m^{α} is the mobile dislocation density for slip system α, and l_{struct} is the mean dislocation path. Furthermore, $T=300\text{K}$ is the temperature, $k_b=8.314\text{JK}^{-1}\ \text{mol}^{-1}$ is the Boltzmann constant, $b=2.5\times10^{-10}$ μm is the Burgers vector, and $\nu_G=10^{12}\ \text{s}^{-1}$ corresponds to the lattice vibration frequency. Dislocation mobility is controlled by the glide activation energy under zero effective shear stress $F_0=0.93$ eV, the thermal slip resistance at 0K $s_t^0=90\text{MPa}$, and the profile parameters $p=1, q=1.5$. Finally, $C_{11}=249\text{GPa}$, $C_{12}=155\text{GPa}$, and $C_{44}=114\text{GPa}$ correspond to the elastic constants with cubic symmetry at room temperature and at 0K $C_{44}^0=128\text{GPa}$.

Dislocation glide is controlled by the effective stress (τ_{eff}^{α}), which corresponds to the macroscopic shear stress less the internal back stress (B^{α}),

$$\tau_{eff}^{\alpha}=\tau^{\alpha}-B^{\alpha}. \tag{2}$$

The athermal or threshold stress (S^{α}) depends on three contributions:

$$S^{\alpha}=S_0^{\alpha}+\alpha_{LE}\frac{\mu b}{d_{struct}}+\mu b\left(A_{\alpha\alpha}\rho_m^{\alpha}\right)^{1/2}. \tag{3}$$

Here, the first term corresponds to the lattice thermal friction $(S_0^{\alpha}=4MPa)$, which is negligible in FCC metals compared to the contributions from dislocation interactions. The second term corresponds to the bow-out stress and assumes irreversible deformation will not occur before a bow-out reaches a critical length (d_{struct}). This term depends on b, the shear modulus $(\mu=80.6\text{GPa})$, and the line energy factor $(\alpha_{LE}=0.5)$. The third term corresponds to the dislocation-dislocation interaction strength for dislocations on the same slip system and depends on μ, and $A_{\alpha\alpha}=0.122$.

The mean dislocation path corresponds to the typical dislocation substructure size, which follows the principle of similitude:[54]

$$d_{struct}=l_{struct}=\frac{K\mu b}{\tau^{\alpha}}, \tag{4}$$

in which $K=8$ corresponds to the with a proportionality constant.[49]

The mobile dislocation density is computed following the balance rate:

$$\dot{\rho}_m^{\alpha}=\left[\frac{1}{b l_{struct}}-\frac{2y_e}{b}\rho_m^{\alpha}\right]|\dot{\gamma}^{\alpha}| +\frac{d_{struct}}{d_0 t_0}\left(\phi_{cs}\rho_m^{\zeta}e^{-\frac{2e4b^3\frac{\mu b}{4\pi y_s}-\tau^{\alpha}}{\tau^{\alpha}\ k_B T}}-\rho_m^{\alpha}e^{-\frac{2e4b^3\frac{\mu b}{4\pi y_s}-\tau^{\zeta}}{\tau^{\alpha}\ k_B T}}\right). \tag{5}$$

The first term corresponds to dislocation multiplication and annihilation, while the second term corresponds to the probability of cross slip of mobile dislocations from plane α to ζ. In addition, $y_e=2$ nm corresponds to the edge dislocation annihilation distance, $y_s=13$ nm is the screw dislocation annihilation distance, and $d_0=1$ μm, $t_0=1$ s, $\phi_{cs}=0.5$ are the cross slip reference distance, time, and efficiency, respectively.

During plastic deformation, the generation, glide, and annihilation of dislocations control the mechanical responses of metallic materials. In metals, immobile dislocations localize and form mesoscale structures with high dislocation densities.[55,56] Regions of high dislocation densities are significantly stiffer, which induce a local

back stress and constrain deformation on low dislocation density areas. In the cases of cyclic loading, these structures organize after a few hundred cycles and are responsible for the development of a back stress upon unloading. For monotonic loading, cell structures become well organized at the onset of Stage II.[57]

The back stress, responsible for directional (kinematic) hardening, depends on the constraint imposed by high density of immobile dislocations[58] and is computed as,

$$\dot{B}^{\alpha} = \frac{f_w}{1-f_w}\frac{2\mu(1-2S_{1212})}{(1+4\mu S_{1212} f_{Hill})}\gamma^{\alpha}. \tag{6}$$

The wall fraction (f_w) decreases with the accumulated plastic shear strain according to[59]

$$fw = f_{inf} + \left(f_0 - f_{inf}\right)\exp\left(\frac{-\gamma_p}{g_p}\right), \tag{7}$$

and the accommodation factor f_{Hill}[60] is defined as

$$f_{Hill} = (1-f_w)\left(1-\frac{d_{struct}}{d_{gr}}\right)\left(\frac{d\gamma^{\alpha}}{d\tau^{\alpha}}\right). \tag{8}$$

S_{1212} corresponds to the shear component of the Eshelby tensor for a sphere[61]

$$S_{1212} = \frac{(4-5\nu_p)}{15(1-\nu_p)} \tag{9}$$

with

$$\nu_p = \frac{\nu + \frac{2}{3}\mu(1+\nu)f_{Hill}}{1+\frac{4}{3}\mu(1+\nu)f_{Hill}}, \tag{10}$$

in which $\nu = 0.3$ corresponds to the Poisson modulus. Formulations akin to Equations 6 and 7 were shown[62] to result in hardening-recovery response (also known as Frederick-Armstrong).

We highlight that the accommodation factor (Equation 8) conveys the influence from the grain size (d_{gr}). Such a dependence is indeed expected from the mean-field approach behind Equation 6 since the domain in which a dislocation structure sits (e.g., a cell) is not infinite, as assumed by Eshelby.[63] Therefore, for grain sizes about the size of dislocation structures, f_{Hill} is reduced, which increases the macroscopic stress. As the grain size increases with respect to the dislocation structure length scale, the strengthening dilutes, and the infinite domain becomes a good approximation. This mechanisms is able to reproduce the observed grain size sensitivity, which peaks at intermediate strains and reduces upon further deformation due to the refinement of dislocation structures.[64]

We note that our approach is generic for FCC metals with medium to high stacking fault energies, but we use material properties previously identified for pure nickel[48]; the reader is referred to the original work for further details about the determination of parameters. Furthermore, initial parameters used in this model are the initial density of mobile dislocations, $\rho^s_{m0} = 10^{10}$ m^{-2}, and the initial structural distance $d_{struc} \sim 10$ μm. Although these initial conditions are likely to depend on the grain size, texture, and microstructure morphology, we make the simplifying assumption that the same initial values apply for all cases.

To demonstrate the response of the constitutive model, we performed finite element simulation using the polycrystalline prismatic mesh in Figure 2, which contains 500 randomly oriented grains. We applied quasi-static displacement-control deformation along the X axis, and the results for different grain sizes are reproduced in Figure 3 (left and center). Comparing these results with experiments, Figure 3 (right), simulations reproduce the increase in stress upon a reduction in grain size and the saturation of the grain size effects above a few hundred microns. We acknowledge that a perfect fit to experiments is beyond the scope of this work, but it is most likely unnecessary to identify generalities across FCC metals. We also note that the model has limited grain size sensitivity at yield (i.e., Hall-Petch effect), which is likely due to identical initial conditions for all models.

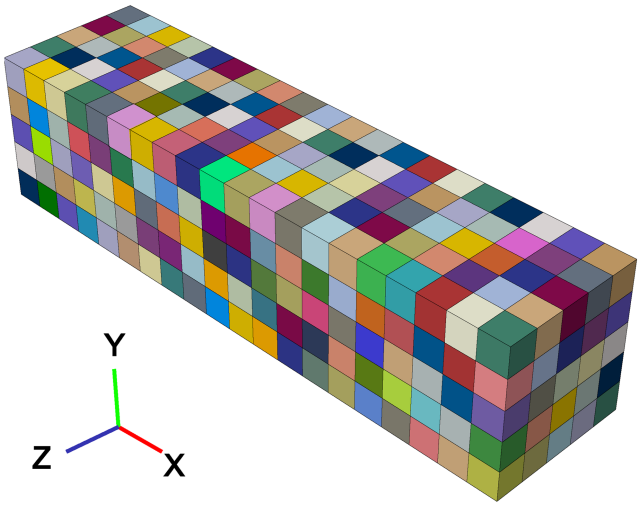


FIGURE 2 Finite element model employed for modeling the macroscopic stress-strain response. Colors correspond to different grains [Colour figure can be viewed at wileyonlinelibrary.com]

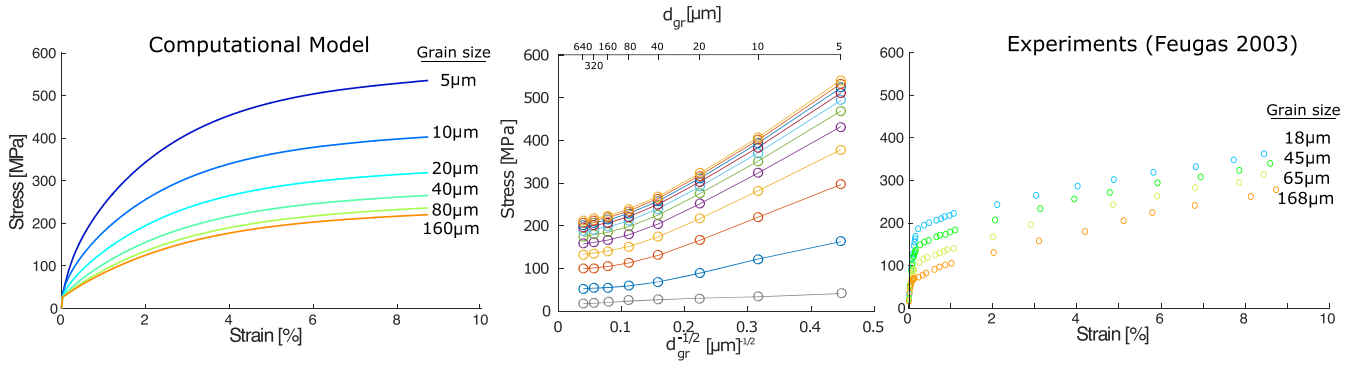


FIGURE 3 Engineering stress-strain curves for various grain sizes from crystal plasticity models (left and center) and experiments[64] (right) [Colour figure can be viewed at wileyonlinelibrary.com]

2.2 | Finite element meshes with cracks

We consider finite element meshes with a "long crack" of length to width ratio of $a/w = 0.5$ and a semi-circular tip formed by 16 elements (Figure 4), typical of elasto-plastic fracture mechanics models. The initial crack opening is 10% of the specimen side, which limits the need for mesh refinements and therefore the total number of elements. The finite element model is made of 9,646 3D hexahedral ("brick") elements with a single element through the thickness. There is no out-of-plane constraint in order to represents a plane stress condition, typical of thin sheets.

To mitigate mesh sensitivity, we consider driving forces that avoid measuring internal state variables at highly strained elements (which are sensitive to mesh refinement). Instead, we estimate the fracture driving force based on the crack mouth displacement (CMD), the crack tip displacement (CTD), and the displacement at a distance of one crack tip radius ahead of the crack (δ_A), which resembles the δ_5 proposed by Schwalbe.[65] Figure 4 details the exact nodes at which these displacements were computed. Note that CTD usually has little sensitivity to mesh refinement and crack tip morphology[66] compared to the most strained elements at the crack tip. Appendix A presents a brief mesh convergence study that justifies the choice of discretization. More detailed mesh convergence studies in crystal plasticity finite element simulations can be found elsewhere.[67,68]

Uniaxial loading is applied via quasi-static force or displacement increments at the right side of the mesh, and in the X-axis direction (Figure 4), while the left side is constrained in the X axis. Upon reaching the maximum load or displacement in 2 s, the opening (X) and sliding (Y) components of the CTD, CMD, and δ_A are computed. Under displacement control, we apply a nominal deformation of 2% and under force control, the maximum load yields crack tip openings similar to those under displacement control with a grain size of 100 μm. All other boundaries are free of constraint, and nodes along those boundaries are free to displace.

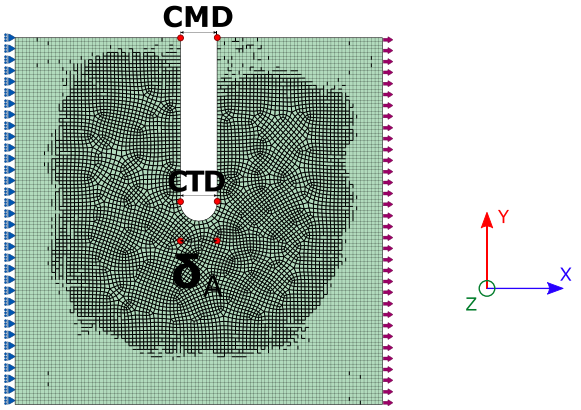


FIGURE 4 Finite element mesh composed of 3D hexahedral element; thickness is one element. Loading and constraint along X direction are presented. The highlighted nodes correspond to those used for measuring displacements at the mouth of the crack (CMD), at the tip of the crack (CTD), and at a distance of one crack tip radius ahead of the crack (δ_A) [Colour figure can be viewed at wileyonlinelibrary.com]

2.3 | Microstructure arrangements

We consider four microstructure arrangements, each with approximately 1,000 equiaxed grains as shown in Figure 5: (a) isotropic equiaxed grains, (b) decreasing grain size towards X direction, (c) decreasing grain size towards Y direction, and (d) radially increasing grain size towards the crack tip. These gradients correspond to a grain size reduction by a factor of 4 between extremes. These polycrystalline microstructures were generated from the kinetic Monte Carlo (kMC) Potts grain growth model[69,70] and finite element mesh using three-dimensional hexahedral elements. Random initial crystal orientations are assigned to each grain.

For each grain, we computed a nominal grain diameter based on the total volume of an equivalent spherical grain. In addition, we consider synthetic gradients in crystallographic orientation along X, Y, and radial direction (see the axis in Figure 4). These microstructures consider a linear gradient in grain orientations starting from a perfect single crystal to random orientations. Figure 6 depicts grains colored with IPF value with respect to the X direction and demonstrates the gradient in crystallographic orientation from a single value (single crystal) to random orientation (non-textured polycrystal).

3 | SIMULATION RESULTS

Next, we present the results from microstructure-sensitive models, isotropic elastic models, and isotropic elasto-plastic models constructed with the piece-wise stress-strain curve in Figure 3 and von Mises yield surface criteria.[51]

3.1 | Opening and sliding results for homogeneous equiaxed grains

We first evaluate ten equiaxed microstructures (Figure 5A) with mean grain size 5 or 100 μm under displacement control. All simulations are equivalent except for the random allocation of grain dimensions, locations, and orientations. Furthermore, we consider the change in the displacement (Δ) rather than the total displacement since the latter has an artificial opening contribution from the initial crack morphology. Hence, the range is appropriate for representing the sensitivity of microsplasticity on microstructure.

Figure 7 depicts the change in crack mouth displacement (ΔCMD), crack tip displacement (ΔCTD), and displacement ahead of the crack tip ($\Delta\delta_A$) upon loading. These results demonstrate that under displacement control, the ΔCMOD is insensitive to the microstructure while ΔCTOD and $\Delta\delta_A$ can be affected by the microstructure. Furthermore, microstructure-sensitive models

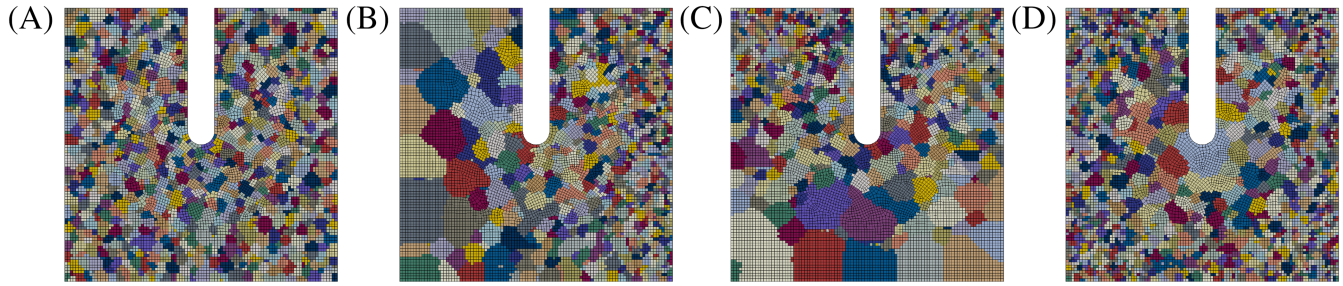


FIGURE 5 Finite element meshes of polycrystalline microstructures: (A) Isotropic equiaxed grains, (B) Decreasing grain size towards X direction, (C) decreasing grain size towards Y direction, and (D) radially increasing grain size towards the crack tip. Colors indicate different grain orientations [Colour figure can be viewed at wileyonlinelibrary.com]

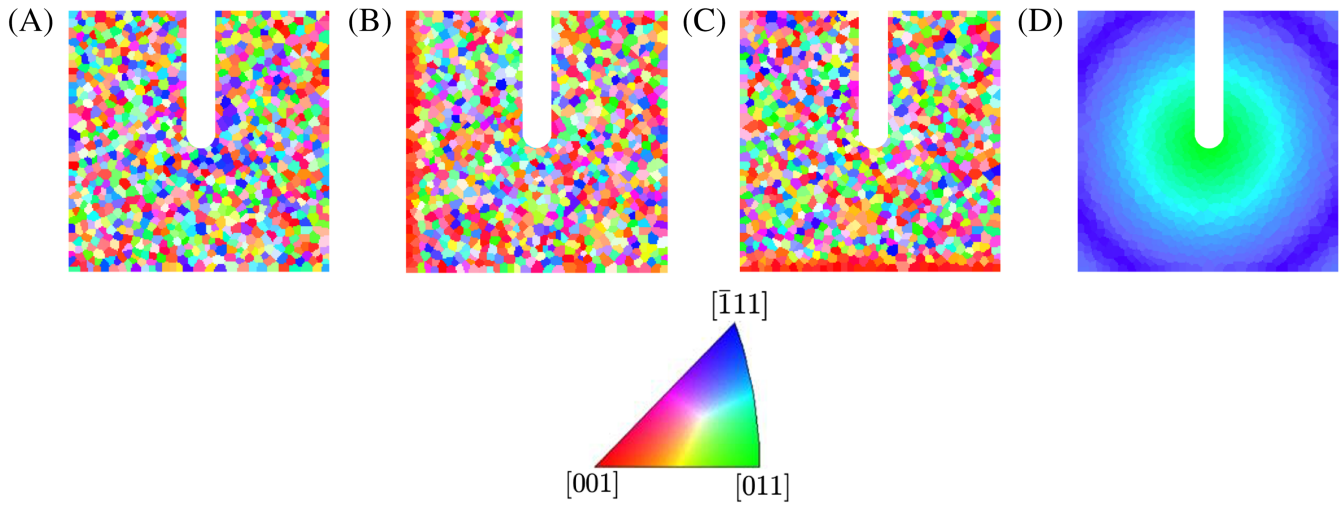


FIGURE 6 Crystallographic orientation: (A) random, (B) X-axis gradient, (C) Y-axis gradient, and (D) radial gradient. Colors indicate IPF value with respect ot the X direction. The linear gradients correspond to gradients from [001] oriented to random. The radial gradient corresponds to [011] oriented at the crack tip to [111] oriented at the boundary [Colour figure can be viewed at wileyonlinelibrary.com]

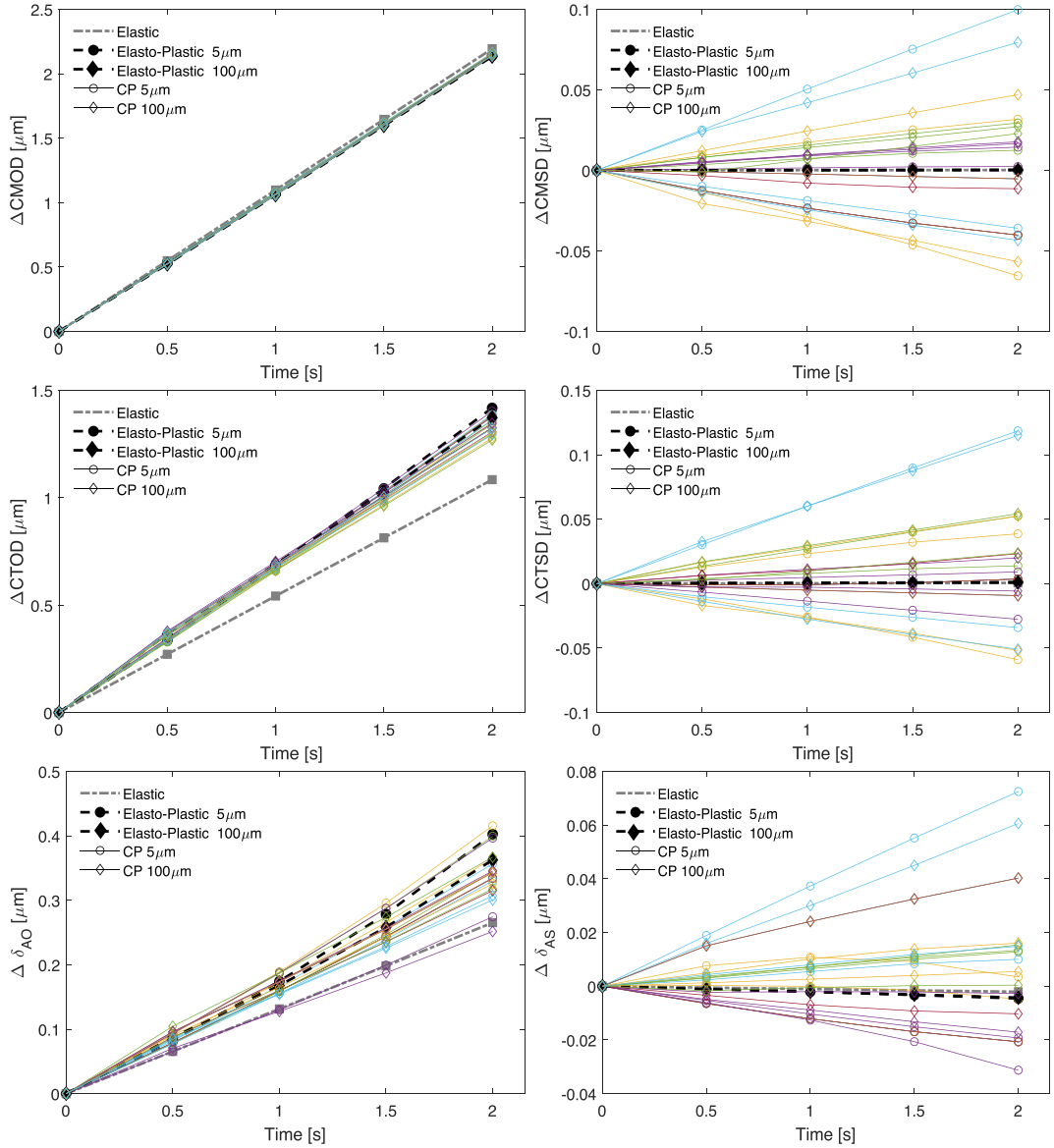


FIGURE 7 Opening (left) and sliding (right) components of the ΔCMD, ΔCTD, and $\Delta\delta_A$ under displacement control. Colors correspond to 10 equiaxed microstructural realizations, while black corresponds to homogeneous isotropic plastic model. The use of the change in the displacement (Δ) mitigates the arbitrary choice for the initial crack opening [Colour figure can be viewed at wileyonlinelibrary.com]

present non-negligible sliding displacements (Mode II deformation) even though isotropic plastic models predict no shear.

Figure 8 presents opening and sliding displacements results under force control for the same microstructures in Figure 7. The maximum applied force is such that the CTD for 100 μm grain size is similar to that computed under displacement control. As a result, the crack displacements under force and displacement control are similar for a 100 μm grain size. However, under force control, displacements are different for both grain sizes. Again, all microstucture-sensitive results present significant variability that deviates from the isotropic elasto-plastic model.

Figure 9 compares the stress and strain fields from one microstructure realization with different mean grain size (note the same color scale was used for both grain sizes). Upon deforming with a nominal strain of 2%, the strain fields are similar for both grain sizes (Figure 9A,B), but the stress fields differ in magnitude (Figure 9C,D); hence, the elastic strains are significantly different. Above a nominal strain of 0.1%, elastics strains are negligible, and the total and plastic strains are similar. When the total strain fields are similar for both grain sizes, the CTODs are indistinguishable. When the same force is applied to both grain sizes, the stress (Figure 10A,B) and the elastic strains fields are similar. However, the total strains are significantly different due to the

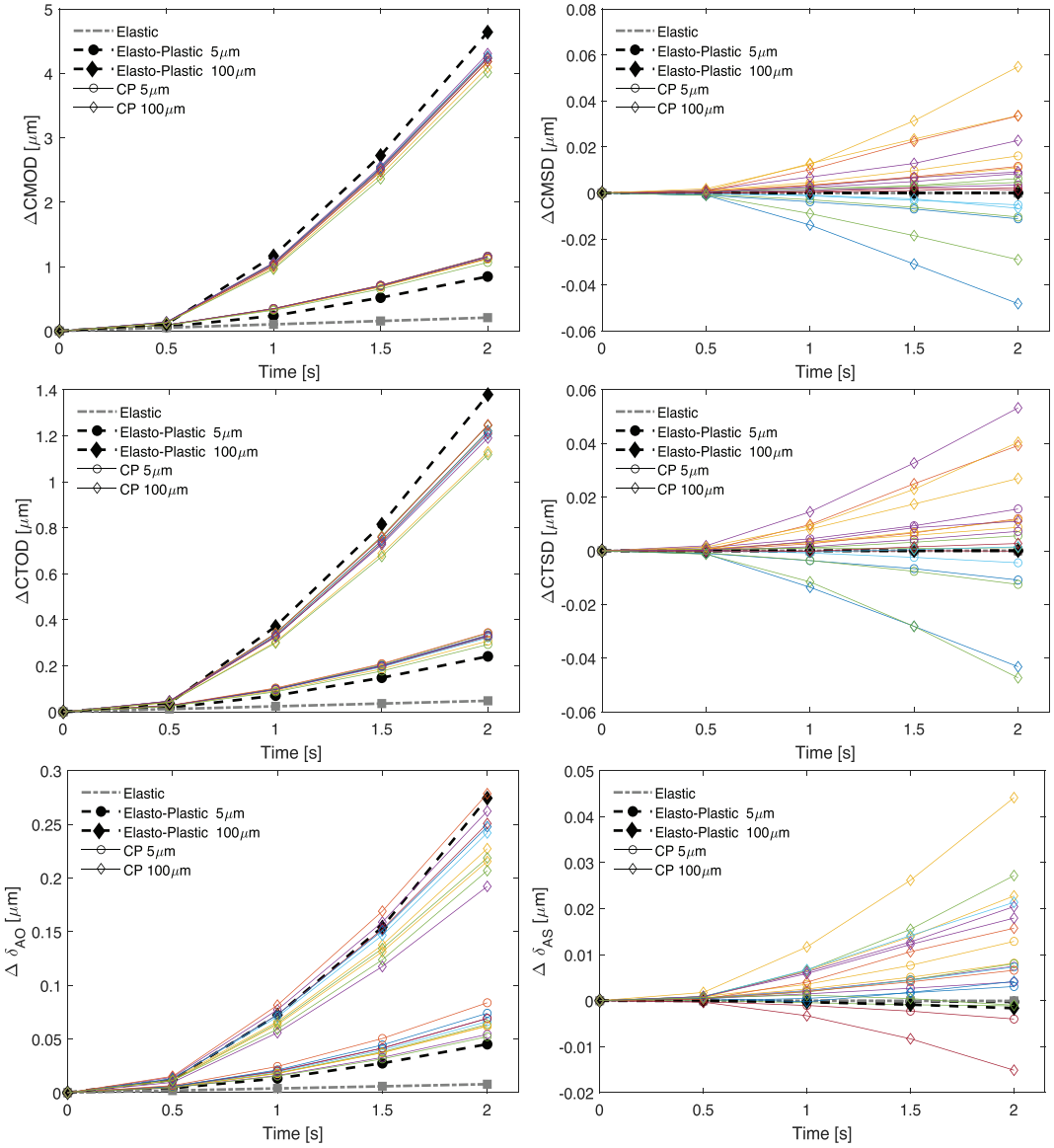


FIGURE 8 Opening (left) and sliding (right) components of the ΔCMD, ΔCTD, and $\Delta\delta_A$ under force control. Colors correspond to 10 equiaxed microstructural realizations, while black corresponds to homogeneous isotropic plastic model [Colour figure can be viewed at wileyonlinelibrary.com]

strengthening effects of the smaller grain size; this difference results in CTODs with a marked difference.

Figure 11 summarizes the normalized distributions of ΔCMD, ΔCTD, and $\Delta\delta_A$ at peak load under force control. Multiple equiaxed microstructural realizations are considered with two grain sizes (elastic results are not included). The normalization factor is the average opening displacement for the corresponding grain size. The results show some clear trends:

- The normalized variability of $\Delta\delta_A$ is higher than that for ΔCTD, which is still higher than that for ΔCMD. Thus, the closer we measure the displacement from the crack tip, the larger variability.
- The variability is significantly lower for ΔCMSD than for ΔCMOD. On the contrary, opening and sliding components of $\Delta\delta_A$ have similar variability. Such a difference suggests that far field measurements of the fracture driving force smear out the Mode II component compared to Mode I.
- The normalized displacements are consistently lower for the largest grain size, which is the result of the saturation of grain size effects towards large grains.

Figures 7 and 8 demonstrate that the microstructure has an important effect on the variability of the fracture driving force. Furthermore, force control models are sensitive to the grain size, which justifies that we proceeded

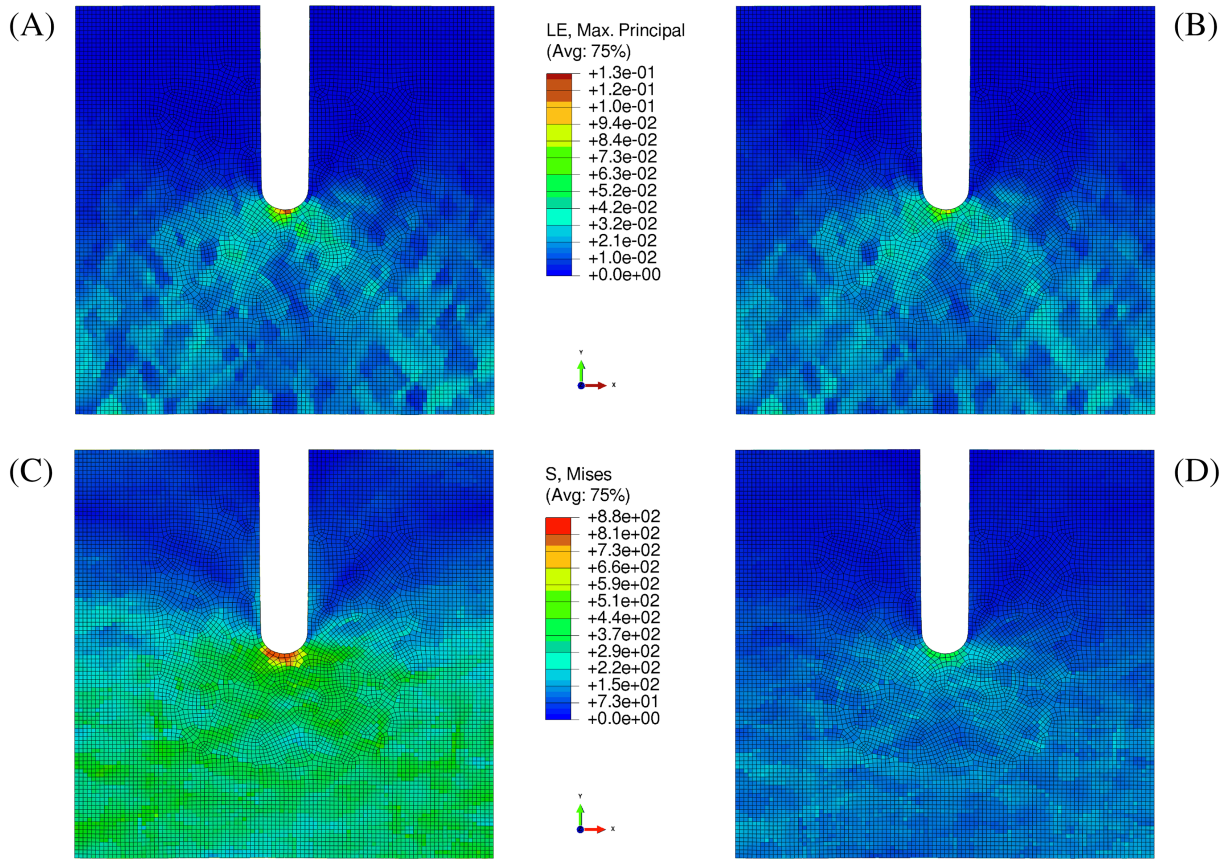


FIGURE 9 Example of the strain and stress fields for one realization with equiaxed grains under displacement control. (A and B) total engineering strain and (C and D) von Mises stress for 5 and 100 μm grain sizes, respectively. Note the same color scale used for both grain sizes [Colour figure can be viewed at wileyonlinelibrary.com]

by focusing on force control simulations. Displacement controlled models would yield similar results to those presented next upon loads that lead to the same nominal displacements; these load would be depend on the mean grain size.

3.2 | Opening and sliding results for domains with grain size gradients

Figure 12 presents the peak normalized opening and sliding displacements under force control from models with a linear decrease in grain size along the X axis (i.e., parallel to the loading direction, Figure 5B). The normalization factor corresponds to the average opening displacement from equiaxed microstructure loading under identical conditions. We also consider simulations with average grain sizes of 5 or 100 μm.

Compared to equiaxed isotropic microstructures (Figure 11), microstructure gradients along the X axis in Figure 12 have a notable effect on the mean value and variability of ΔCMD and ΔCTD. In addition, the microstructure gradient induces an evident shear displacement towards one direction. The results further show that the microstructure with a larger average grain size has a smaller bias and variability. We attribute this to the saturation of the grain size effect for large grains (greater than 100 μm). Thus, gradients and size effects are intrinsically coupled.

Figure 13 presents the normalized displacements at peak load under force control for microstructure gradients along the Y axis (i.e., perpendicular to the loading direction, Figure 5C). Again, displacements were normalized by the corresponding opening values from equiaxed microstructure. Compared to Figure 11, gradients along Y axis induce larger opening displacements (note normalized values are over 1), which is due to the presence of larger grains that present lower resistance. Shear displacements have a slightly larger variability compared to equiaxed microstructures, and they are biased from zero (i.e., there is a driving force to turn the crack). Microstructures with 100 μm average grain size again have smaller variability and bias from zero due to grain size effect saturation.

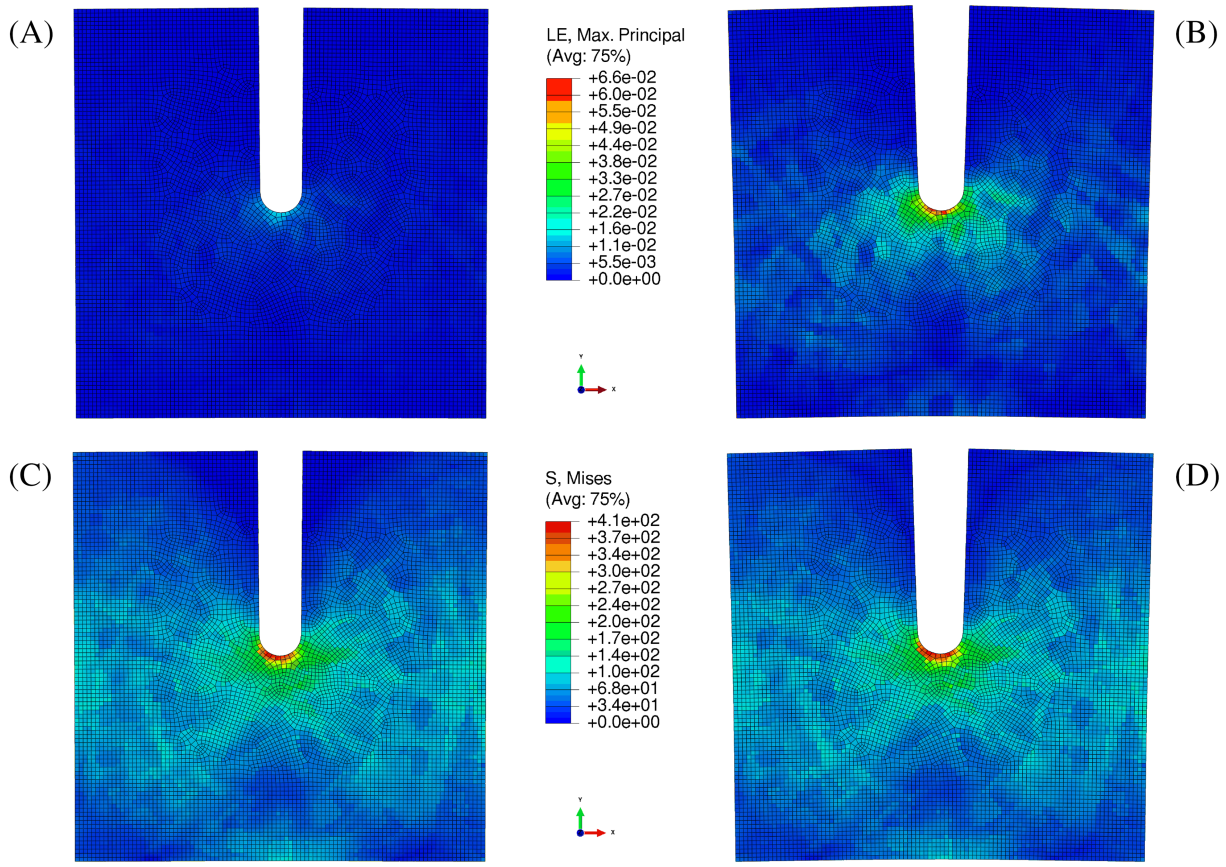


FIGURE 10 Example of the strain and stress fields for one realization with equiaxed grains under force control. (A and B) total engineering strain and (C and D) von Mises stress for 5 and 100 μm grain sizes, respectively. Note the same color scale used for both grain sizes [Colour figure can be viewed at wileyonlinelibrary.com]

Figure 14 summarizes the opening and sliding displacements for radial microstructural gradients (Figure 5D) at peak load under force control. In addition to an increase in the displacements due to the larger grains, there is a significant increase in variability. Contrary to the previous analysis with gradients, there is no shear preferential direction, which suggest that the crack would grow in Mode I. Again, results from larger grain size average show lower bias from zero and variability.

3.3 | Opening and sliding results for crystallographic orientation gradients

We now consider the effects of three different crystallographic orientation gradients (Figure 6) under force control for 10 equiaxed microstructures with 5 μm mean grain size. The orientation change linearly from random orientation (no texture) at the center to single crystal orientations such that the lattice vectors [001], [011], or [111] are oriented along the loading axis (X axis). These orientations were chosen to investigate the role of the high elastic anisotropy of nickel. The Young's modulus varies from 130 GPa for crystals oriented along [001] direction to about 220 GPa for crystals deformed along [011] and 290 GPa for [111] orientation.

Figures 15 and 16 present the normalized opening and sliding displacement at peak load for crystallographic gradients along X axis and Y axis, (Figure 6B,C, respectively); the normalization factor is the corresponding opening displacement for [001] orientation. The results demonstrate that X-axis grain orientation gradients can bias ΔCMSD and ΔCTSD from zero and result in local shear. The results for $\Delta\delta_A$ do not present a clear trend, which would suggest that the orientation of the grain at the crack tip dominates this displacement measure.

Finally, Figure 17 presents the normalized displacements for equiaxed microstructures with radial crystallographic orientation gradients (Figure 6D). In these simulations, grain orientation shifts from [001] being aligned along the X axis at the crack tip to [111] alignment with X axis at the outer boundary, and vice-versa. Furthermore, the normalization factor is the corresponding opening displacement for [001]

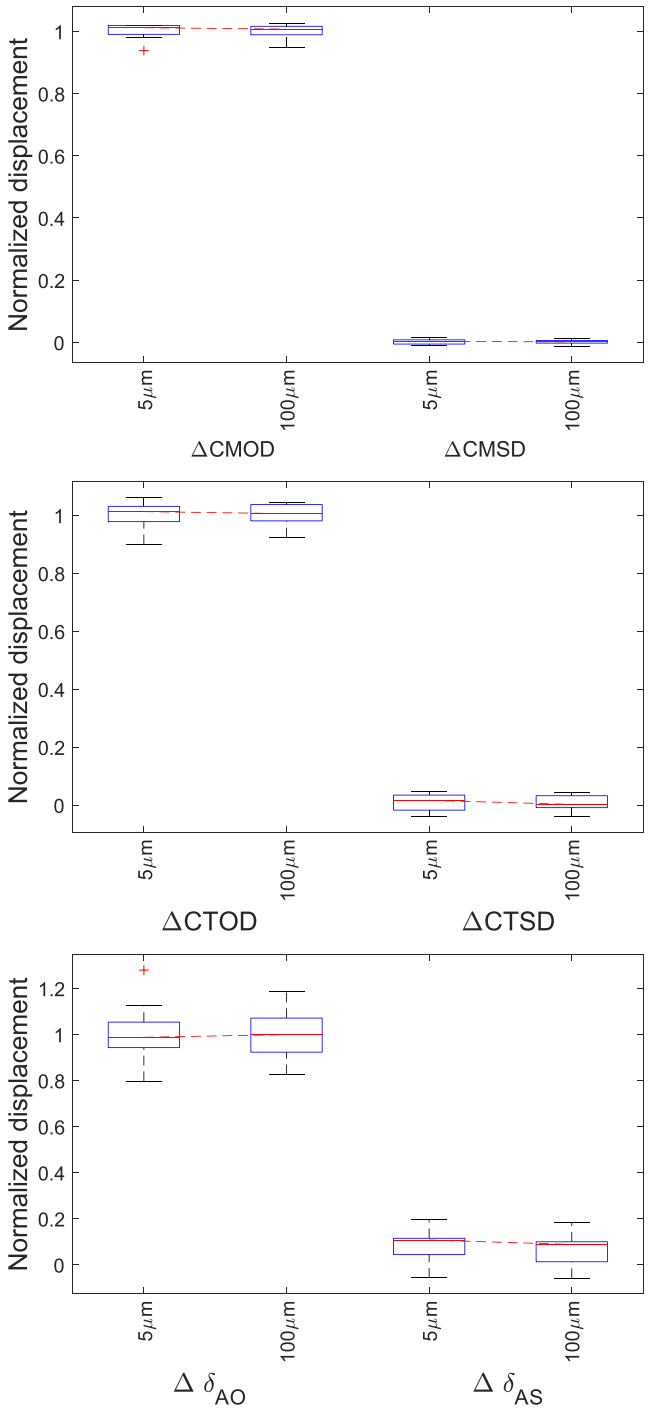


FIGURE 11 Boxplots summarizing normalized distributions of maximum ΔCMD, ΔCTD, and $\Delta\delta_A$ values for multiple equiaxed microstructural realizations under force control. Red lines represent mean values, blue boxes represent 25th and 75th percentiles, and black lines correspond to outliers. The normalization factor corresponds to the average opening displacement for each grain size [Colour figure can be viewed at wileyonlinelibrary.com]

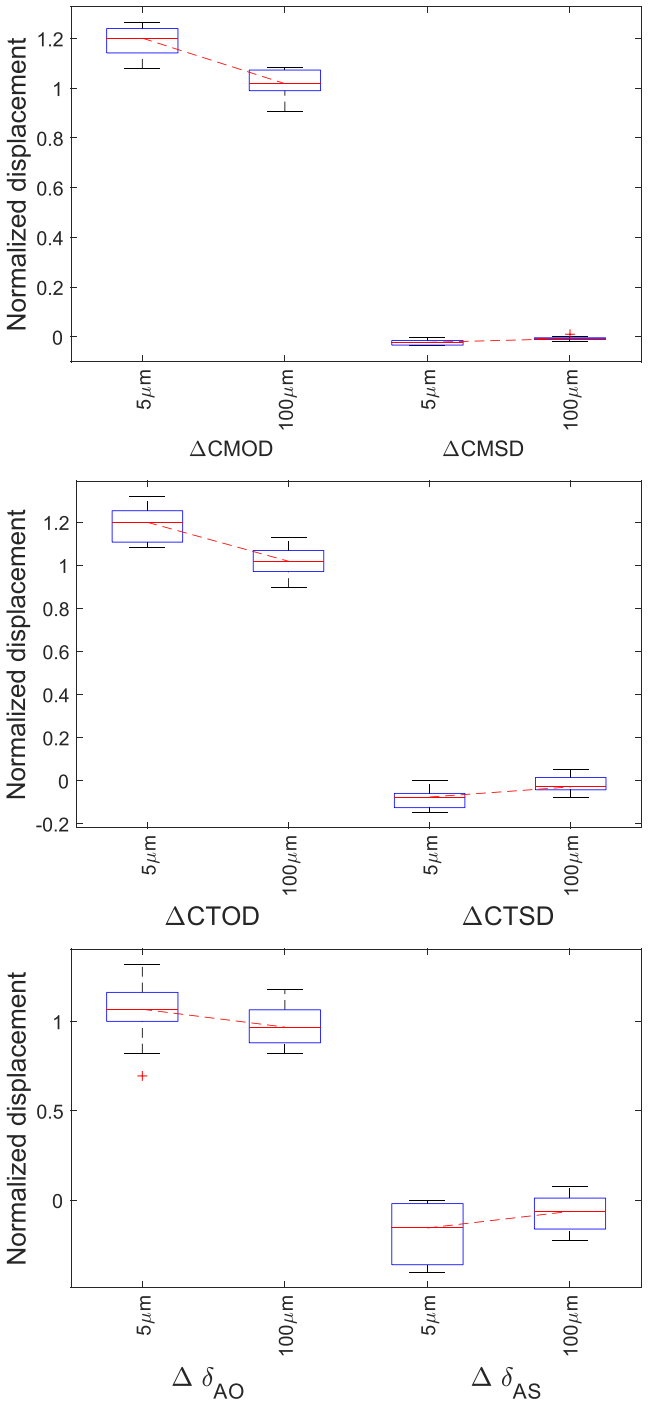
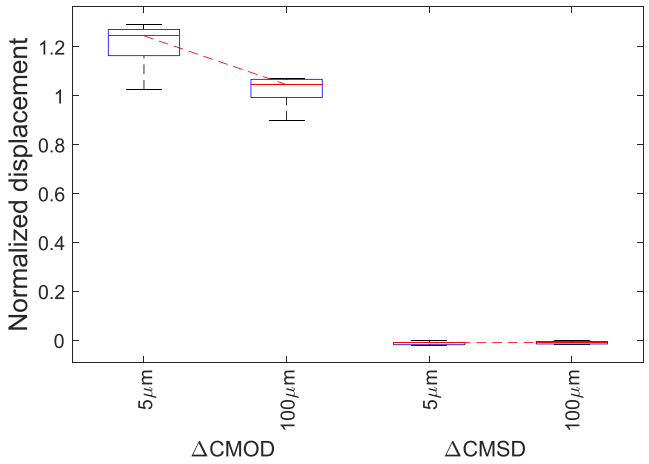
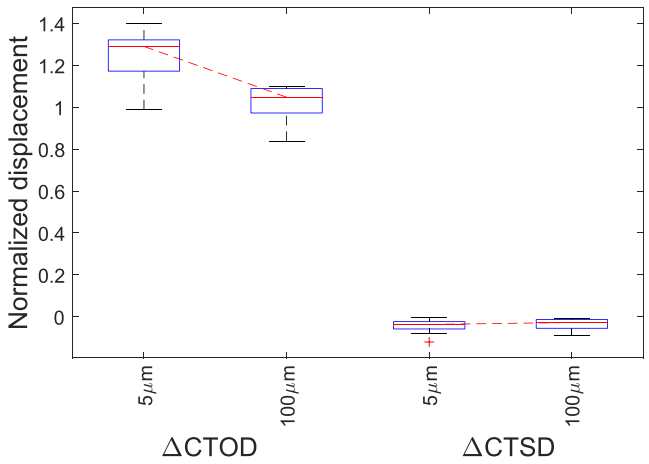


FIGURE 12 Boxplots summarizing normalized distributions of peak ΔCMD, ΔCTD, and $\Delta\delta_A$ values for multiple microstructural *X*-axis gradients realizations under force control. Red lines represent mean values, blue boxes represent 25th and 75th percentiles, and black lines correspond to outliers. The normalization factor corresponds to the average opening displacement from equiaxed microstructure for each grain size [Colour figure can be viewed at wileyonlinelibrary.com]

orientation. Overall, the results demonstrate that the crystallographic orientation at the crack tip dominates the opening displacement components. On the contrary, shear components are influenced by the neighborhood away from the crack tip. Furthermore, the results for simulations with single crystals (not shown) present similar





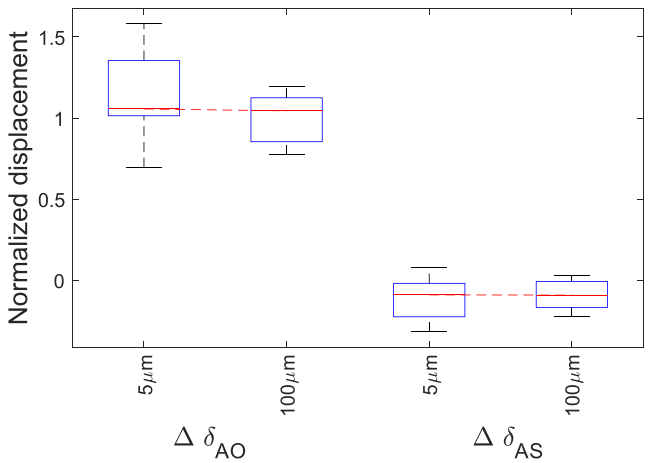
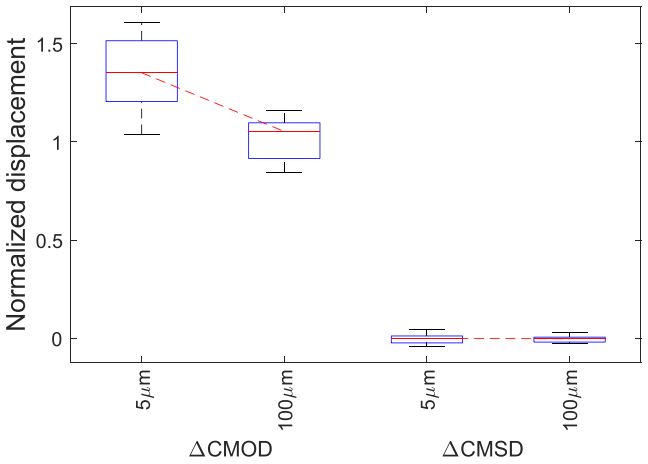
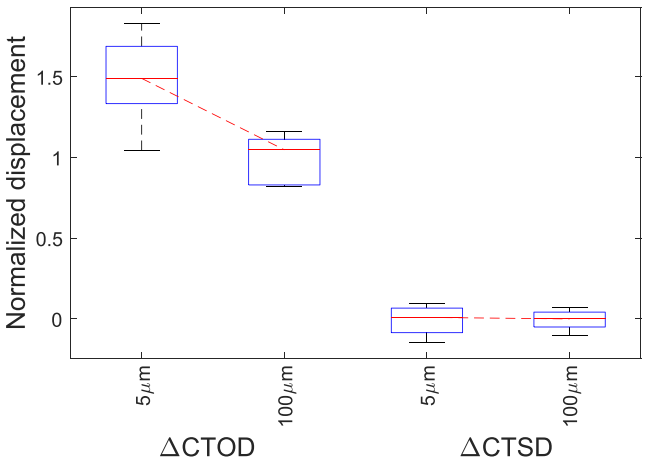


FIGURE 13 Boxplots summarizing normalized distributions of maximum ΔCMD, ΔCTD, and $\Delta\delta_A$ values for multiple microstructural *Y*-axis gradients realizations under force control. Red lines represent mean values, blue boxes represent 25th and 75th percentiles, and black lines correspond to outliers. The normalization factor corresponds to the average opening displacement from equiaxed microstructure for each grain size [Colour figure can be viewed at wileyonlinelibrary.com]





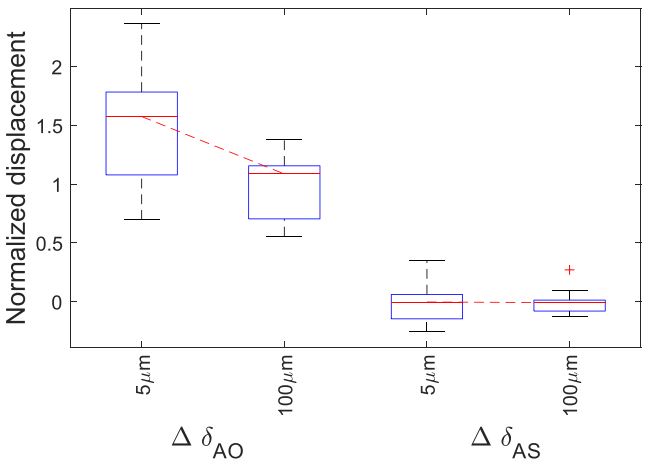


FIGURE 14 Boxplots summarizing normalized distributions of peak ΔCMD, ΔCTD, and $\Delta\delta_A$ values for multiple microstructural *R*-axis gradients realizations under force control. Red lines represent mean values, blue boxes represent 25th and 75th percentiles, and black lines correspond to outliers. The normalization factor corresponds to the average opening displacement from equiaxed microstructure for each grain size [Colour figure can be viewed at wileyonlinelibrary.com]

opening and sliding trends: whereas the [001] orientation presents almost no shear, the [111] presents strong shear. Hence, the orientation of the grain at the crack tip does not fully explain the displacement variability and the entire microstructure between the local and far fields affect the results.

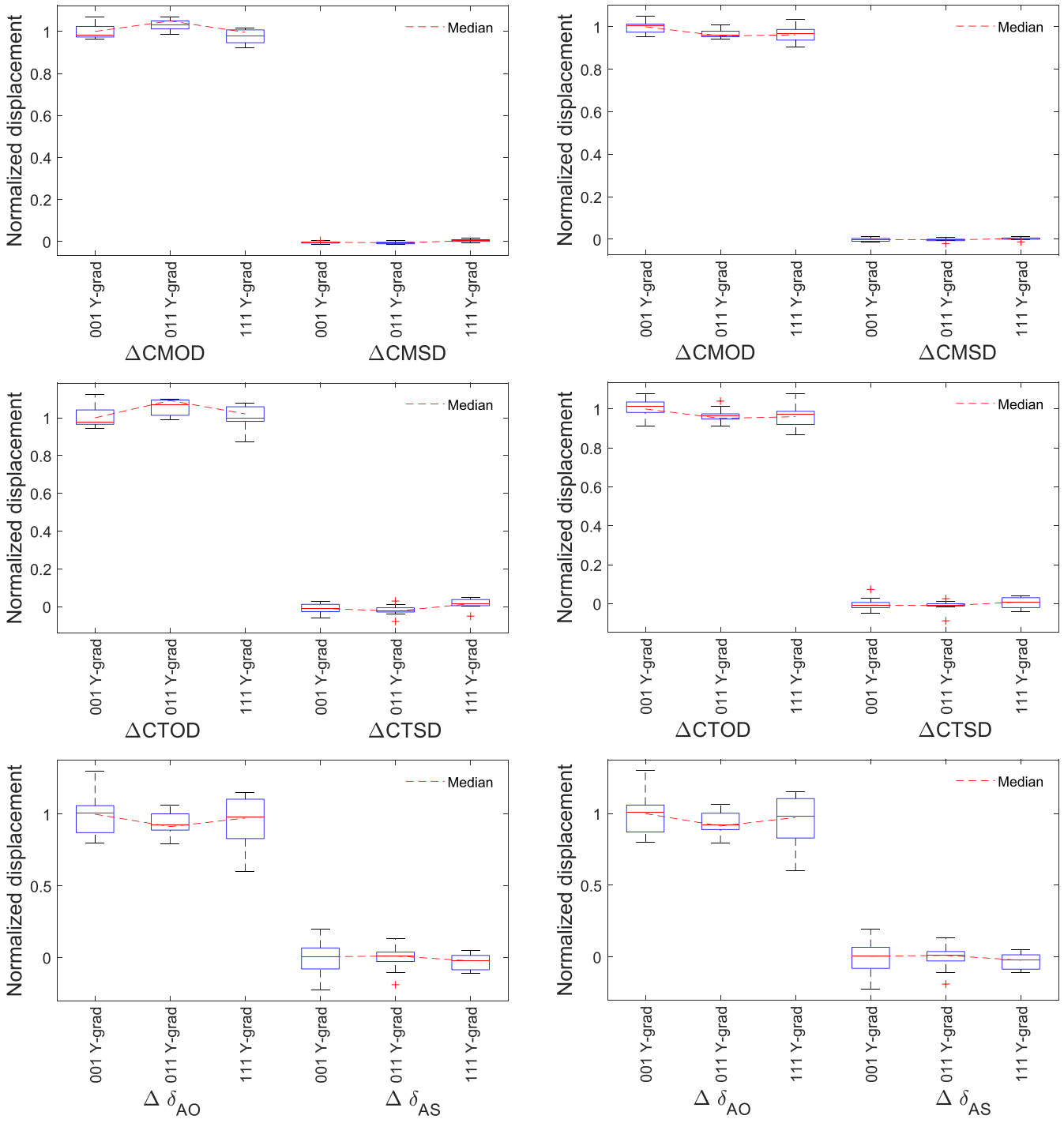


FIGURE 15 Boxplots summarizing normalized distributions of maximum ΔCMD, ΔCTD, and $\Delta\delta_A$ values for multiple texture gradients along *X* axis and mean grain size of 5 μm under force control. The normalization factor is the corresponding opening displacement for [001] orientation [Colour figure can be viewed at wileyonlinelibrary.com]

FIGURE 16 Boxplots summarizing normalized distributions of peak ΔCMD, ΔCTD, and $\Delta\delta_A$ values for multiple texture gradients along *Y* axis and mean grain size of 5 μm under force control. The normalization factor is the corresponding opening displacement for [001] orientation [Colour figure can be viewed at wileyonlinelibrary.com]

4 | DISCUSSION

This work demonstrate that the interaction among ductile strengthening mechanisms and microstructural attributes affects the crack tip response. We employed a crystal plasticity constitutive model to describe mesoscale heterogeneity, and we quantified the effects of microstructure gradients on crack tip microplasticity. In addition, our

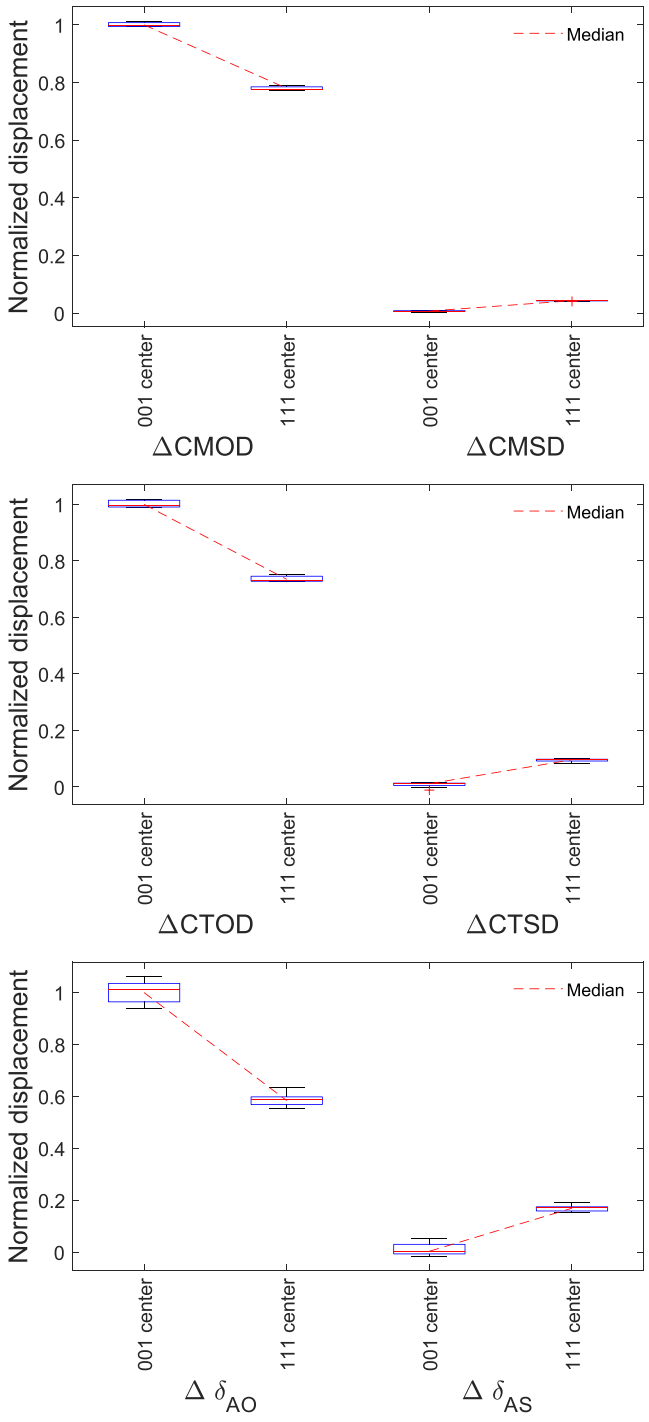


FIGURE 17 Box plots summarizing normalized distributions of maximum ΔCMD, ΔCTD, and $\Delta\delta_A$ values for radial crystallographic gradients and mean grain size of 5 μm under force control. The normalization factor is the corresponding opening displacement for [001] orientation [Colour figure can be viewed at wileyonlinelibrary.com]

calculations estimated the intrinsic variability of crack blunting induced by microstructural attributes.

Microstructures-sensitive models resulted in negligible CMOD variability, which agrees with homogeneous isotropic plastic models (Figure 11). On the contrary, CTOD is significantly influenced by the microstructure, and the effects are more significant close to the crack tip. These results would suggest that the plastic hinge model[71] used to infer CTOD from CMOD measurements can smear out the local variability. Hence, the plastic hinge model may be suboptimal for understanding and characterizing stochastic failures from moderate fracture toughness materials such as welded, additive manufactured, or materials with brittle to ductile transition.[72]

The results further showed that microstructure can induce significant Mode II displacements at the crack tip while being loaded nominally under Mode I (Figure 11). The shear deformation only occurs in microstructure-sensitive models and depends on the microstructural neighborhood of the crack tip, not just a single grain at the crack tip. Multiple microstructures presented shear displacements equally distributed in both directions, which suggests that cracks would grow normal to the loading direction at the macroscopic scale. However, we infer that microstructures with larger crack tip shear displacements would likely result in a more serrated fracture surfaces and better fracture resistance.

We also demonstrated that grain size and orientation gradients influence the crack tip microplasticity and affect local fracture driving forces by modifying their mean value and increasing their variability. Furthermore, we demonstrated that both grain size gradient and grain size average have a role. As a result, some microstructures result in crack tip shear predominantly occurring towards one directions (e.g., Figure 12), which has the potential to improve fracture toughness by turning the crack from Mode I growth. These microstructures could effectively be use to divert crack paths.

The microstructure in the neighborhood of the crack tip explains much of the variability as demonstrated by the results for microstructures with radial gradients (Figures 14 and 17). Since the CTOD changes as a function of the loading level, such a neighborhood is also a function of the applied load. Hence, sensitivity to microstructure should peak at intermediate plastic strains and prior to void formation, which is the regime studied in this work. The exact loading condition that would present maximum sensitivity depends on the CTOD dimension relative to the grain size and the evolution of internal state variables, e.g., dislocation densities and mesoscale structures. These results highlight the importance of considering models that reproduce grain size effects at a wide range of plastic strains, including saturation at large strains.

One limitation of our simulations is the one-element thickness mesh, which could somewhat magnify the sensitivity to microstructure compared to thicker models.

Although a more constrained specimen could potentially help to homogenize the displacements along the crack front, the weakest link that controls failure still depends on a neighborhood much smaller than the crack front. Hence, our results are still relevant for understanding the most significant effects induced by microstructure gradients on crack blunting.

Finally, crystal plasticity models rely on plastic shear and do not include any provision for void formation, growth, and coalescence. We mitigated this limitation by applying loads that results in maximum local plastic strains below 10%. As a result, our analysis does not consider ductile crack propagation, for which appropriate sensitivity to hydrostatic stresses and damage should be included. Nevertheless, our conclusions are relevant in general since we describe the intermediary of microstructure gradients, which undergo relatively low strains in between the local process zone and the far field load.

5 | CONCLUSIONS

This work studied the role of microstructural attributes on crack tip microplasticity. We implemented a systematic microstructure-sensitive approach to compare the effects of grain size and orientation gradients on crack tip microplasticity. The deformation driving forces were surveyed by quantifying the opening and shear displacements at the crack mouth, crack tip, and ahead of the crack. We further compared the results with homogeneous microstructures and isotropic elastic and elastoplastic models.

First, we demonstrated that microstructural variability has a significant effect on crack tip microplasticity. These results can be employed to quantify the resistance against cracking of different microstructures. For example, we would expect that a larger variability would likely result in a more serrated fracture and better fracture resistance. Similarly, a bias in shear displacement has the potential to turn the crack from Mode I growth and divert crack paths.

Second, we showed that the orientation of grains adjacent to the crack tip cannot explain the entire variability and the microstructure arrangements in between the local and far fields affect the results. Indeed, the crystallographic orientation in the neighborhood of the crack tip can bias the opening and sliding displacements, and the size of this neighborhood depends on the amount of deformation.

Finally, we demonstrated that microstructural heterogeneity affects each driving force differently. We showed that conventional method that rely on far-field parameters (e.g., CMOD) may be unsuitable to estimate the local driving force since they smear out much of the microstructural variability. As a results, local measurements are more appropriate to quantify the role of microstructure on stochastic fracture.

ACKNOWLEDGMENTS

This work is supported by the Exploratory Express LDRD project 193072, Predicting Performance Margins (PPM) and Advanced Simulation and Computing – Physics and Engineering Models (ASC-P&EM) programs at Sandia National Laboratories. Sandia National Laboratories is a multi-mission laboratory managed and operated by National Technology and Engineering Solutions of Sandia, LLC., a wholly owned subsidiary of Honeywell International, Inc., for the U.S. Department of Energy's National Nuclear Security Administration under contract DE-NA0003525.

AUTHOR CONTRIBUTIONS

All authors contributed to the paper with the proportion on the order of the sequence of the authorship. The work of the paper is supervised by the corresponding author.

DATA AVAILABILITY STATEMENT

The data that support the findings of this study are available from the corresponding author upon reasonable request.

ORCID

Gustavo M. Castelluccio https://orcid.org/0000-0003-4291-0443

REFERENCES

1. Zhu X-K, Joyce JA. Review of fracture toughness (G, K, J, CTOD, CTOA) testing and standardization. *Eng Fract Mech*. 2012;85:1-46.
2. Anderson TL. *Fracture Mechanics: Fundamentals and Applications*. 3rd ed. Boca Raton: CRC Press; 2004.
3. Riemelmoser FO, Pippan R. The J-integral at dugdale cracks perpendicular to interfaces of materials with dissimilar yield stresses. *Int J Fract*. 2000;103(4):397-418.
4. Kolednik O, Predan J, Shan GX, Simha NK, Fischer FD. On the fracture behavior of inhomogeneous materials—a case study for elastically inhomogeneous bimaterials. *Int J Solids Struct*. 2005;42(2):605-620.
5. Simha NK, Fischer FD, Kolednik O, Predan J, Shan GX. Crack tip shielding or anti-shielding due to smooth and discontinuous material inhomogeneities. *Int J Fract*. 2005;135(1):73-93.
6. ASTM E1820-09 Standard test method for measurement of fracture toughness; 2009.
7. BS 7448: Part 4 Fracture mechanics toughness test. Method for determination of fracture resistance curves and initiation values for stable crack extension in metallic materials; 1997.

8. Wilsdorf HGF. The ductile fracture of metals: a microstructural viewpoint. *Mater Sci Eng*. 1983;59(1):1-39.
9. Pineau A, Benzerga AA, Pardoen T. Failure of metals I: brittle and ductile fracture. *Acta Materialia*. 2016;107:424-483.
10. Lasalmonie A, Strudel JL. Influence of grain size on the mechanical behaviour of some high strength materials. *J Mater Sci*. 1986;21(6):1837-1852.
11. Srinivas M, Malakondaiah G, Rao PR. Influence of polycrystal grain size on fracture toughness of and fatigue threshold in armco iron. *Eng Fract Mech*. 1987;28(5):561-576.
12. Pippan R, Hohenwarter A. The importance of fracture toughness in ultrafine and nanocrystalline bulk materials. *Mater Res Lett*. 2016;4(3):127-136.
13. Van der Giessen E, Needleman A. Micromechanics simulations of fracture. *Annu Rev Mater Res*. 2002;32(1):141-162.
14. Roy CJ, Oberkampf WL. A comprehensive framework for verification, validation, and uncertainty quantification in scientific computing. *Computer Methods in Applied Mechanics and Engineering*. 2011;200(25-28):2131-2144.
15. Jiang C, Long XY, Han X, Tao YR, Liu J. Probability-interval hybrid reliability analysis for cracked structures existing epistemic uncertainty. *Eng Fract Mech*. 2013;112-113:148-164.
16. Lewandowski JJ. Modern fracture mechanics. *Philos Mag*. 2013;93(28-30):3893-3906.
17. Bechtle S, Kumar M, Somerday BP, Launey ME, Ritchie RO. Grain-boundary engineering markedly reduces susceptibility to intergranular hydrogen embrittlement in metallic materials. *Acta Mater*. 2009;57(14):4148-4157.
18. Kolednik O, Predan J, Fischer FD, Fratzl P. Bioinspired design criteria for damage-resistant materials with periodically varying microstructure. *Adv Funct Mater*. 2011;21(19):3634-3641.
19. Kolednik O, Predan J, Fischer FD, Fratzl P. Improvements of strength and fracture resistance by spatial material property variations. *Acta Mater*. 2014;68:279-294.
20. Yuan H, Zhang W, Castelluccio GM, Kim J, Liu Y. Microstructure-sensitive estimation of small fatigue crack growth in bridge steel welds. *Int J Fatigue*. 2018;112:183-197.
21. Kumar S, Curtin WA. Crack interaction with microstructure. *Mater Today*. 2007;10(9):34-44.
22. Feng H, Fang QH, Zhang LC, Liu YW. Special rotational deformation and grain size effect on fracture toughness of nanocrystalline materials. *Int J Plast*. 2013;42:50-64.
23. Zeng XH, Hartmaier A. Modeling size effects on fracture toughness by dislocation dynamics. *Acta Mater*. 2010;58(1):301-310.
24. Pardoen T, Hutchinson JW. Micromechanics-based model for trends in toughness of ductile metals. *Acta Mater*. 2003;51(1):133-148.
25. Srivastava A, Ponson L, Osovski S, Bouchaud E, Tvergaard V, Needleman A. Effect of inclusion density on ductile fracture toughness and roughness. *J Mech Phys Solids*. 2014;63:62-79.
26. Srivastava A, Osovski S, Needleman A. Engineering the crack path by controlling the microstructure. *J Mech Phys Solids*. 2017;100:1-20 en.
27. Yang F, Yang W. Crack growth versus blunting in nanocrystalline metals with extremely small grain size. *J Mech Phys Solids*. 2009;57(2):305-324.
28. Zhao Y, Fang Q, Liu Y. Effect of cooperative nanograin boundary sliding and migration on dislocation emission from a blunt nanocrack tip in nanocrystalline materials. *Philos Mag*. 2014;94(7):700-730.
29. Asaro RJ. Micromechanics of Crystals and Polycrystals. In: John W. Hutchinson, Theodore Y. Wu, eds. *Advances in Applied Mechanics*: Elsevier; 1983:1-115.
30. Khan A, Huang S. *Continuum Theory of Plasticity*. New York: Wiley; 1995.
31. Dawson PR. Computational crystal plasticity. *Int J Solids Struct*. 2000;37(1-2):115-130.
32. Roters F, Eisenlohr P, Hantcherli L, Tjahjanto DD, Bieler TR, Raabe D. Overview of constitutive laws, kinematics, homogenization and multiscale methods in crystal plasticity finite-element modeling: theory, experiments, applications. *Acta Mater*. 2010;58(4):1152-1211.
33. Martínez-Pañeda E, Niordson CF. On fracture in finite strain gradient plasticity. *Int J Plast*. 2016;80:154-167.
34. Martínez-Pañeda E, Deshpande VS, Niordson CF, Fleck NA. The role of plastic strain gradients in the crack growth resistance of metals. *J Mech Phys Solids*. 2019;126:136-150.
35. McDowell DL. A perspective on trends in multiscale plasticity. *Int J Plast*. 2010;26(9):1280-1309.
36. Kocks UF, Mecking H. Physics and phenomenology of strain hardening: the FCC case. *Prog Mater Sci*. 2003;48(3):171-273.
37. Esteban-Manzanares G, Martínez E, Segurado J, Capolungo L, LLorca J. An atomistic investigation of the interaction of dislocations with guinier-preston zones in al-cu alloys. *Acta Mater*. 2019;162:189-201.
38. Narayanan S, McDowell DL, Zhu T. Crystal plasticity model for BCC iron atomistically informed by kinetics of correlated kinkpair nucleation on screw dislocation. *J Mech Phys Solids*. 2014;65:54-68.
39. Castelluccio GM, Geller CB, McDowell DL. A rationale for modeling hydrogen effects on plastic deformation across scales in FCC metals. *Int J Plast*. 2018;111:72-84.
40. Kubin L, Devincre B, Hoc T. Modeling dislocation storage rates and mean free paths in face-centered cubic crystals. *Acta Mater*. 2008;56(20):6040-6049.
41. Hussein AM, Rao SI, Uchic MD, Dimiduk DM, El-Awady JA. Microstructurally based cross-slip mechanisms and their effects on dislocation microstructure evolution in FCC crystals. *Acta Mater*. 2015;85:180-190.
42. El-Awady JA. Unravelling the physics of size-dependent dislocation-mediated plasticity. *Nat Commun*. 2015;6:5926.
43. Xia S, El-Azab A. Computational modelling of mesoscale dislocation patterning and plastic deformation of single crystals. *Model Simul Mater Sci Eng*. 2015;23(5):55009.
44. Li H, Sun X, Yang H. A three-dimensional cellular automata-crystal plasticity finite element model for predicting the multiscale interaction among heterogeneous deformation, drx microstructural evolution and mechanical responses in titanium alloys. *Int J Plast*. 2016;87:154-180.
45. Kim JH, Lee M-G, Kang J-H, Oh C-S, Barlat F. Crystal plasticity finite element analysis of ferritic stainless steel for sheet formability prediction. *Int J Plast*. 2017;93:26-45.
46. Grilli N, Janssens KGF, Van Swygenhoven H. Crystal plasticity finite element modelling of low cycle fatigue in FCC metals. *J Mech Phys Solids*. 2015;84:424-435.
47. Grilli N, Janssens KGF, Nellessen J, Sandlöbes S, Raabe D. Multiple slip dislocation patterning in a dislocation-based

crystal plasticity finite element method. *Int J Plast*. 2018;100: 104-121.
48. Castelluccio GM, McDowell DL. Mesoscale cyclic crystal plasticity with dislocation substructures. *Int J Plast*. 2017;98(Supplement C):1-26.
49. Sauzay M, Kubin LP. Scaling laws for dislocation microstructures in monotonic and cyclic deformation of FCC metals. *Prog Mater Sci*. 2011;56(6):725-784.
50. Kubin L, Sauzay M. Persistent slip bands: similitude and its consequences. *Acta Mater*. 2016;104:295-302.
51. ABAQUS. FEM software V6.14, Simulia Corp., Providence, RI, USA,; 2016.
52. Busso EP. Cyclic deformation of monocrystalline nickel aluminide and high temperature coatings. *Ph.D. Thesis*; 1990.
53. Kocks UF, Argon A, Ashby MF. Thermodynamics and kinetics of slip. *Prog Mater Sci*. 1975;19:1-288.
54. Kuhlmann-Wilsdorf D. Theory of workhardening 1934-1984. *Metall Trans A*. 1985;16(12):2091-2108.
55. Kuhlmann-Wilsdorf D. Theory of plastic deformation: Properties of low energy dislocation structures. *Mater Sci Eng A*. 1989; 113:1-41.
56. Kuhlmann-Wilsdorf D. The theory of dislocation-based crystal plasticity. *Philos Mag A*. 1999;79(4):955-1008.
57. Kuhlmann-Wilsdorf D. Chapter 59 the LES theory of solid plasticity. *Dislocations in Solids*: Elsevier; 2002:211-342.
58. Sauzay M. Analytical modelling of intragranular backstresses due to deformation induced dislocation microstructures. *Int J Plast*. 2008;24(5):727-745.
59. Estrin Y, Tóth LS, Molinari A, Bréchet Y. A dislocation-based model for all hardening stages in large strain deformation. *Acta Mater*. 1998;46(15):5509-5522.
60. Berveiller M, Zaoui A. An extension of the self-consistent scheme to plastically-flowing polycrystals. *J Mech Phys Solids*. 1979;26(5-6):325-344.
61. Mura T. *Micromechanics of defects in solids*. Dordrecht: Martinus Nijhoff Publishers; 1987.
62. Hennessey C, Castelluccio GM, McDowell DL. Sensitivity of polycrystal plasticity to slip system kinematic hardening laws for al 7075-t6. *Mater Sci Eng A*. 2017;687:241-248.
63. Eshelby JD. The determination of the elastic field of an ellipsoidal inclusion, and related problems. *Proc R Soc Lond Ser A Math Phys Sci*. 1957;241(1226):376-396.
64. Feaugas X, Haddou H. Grain-size effects on tensile behavior of nickel and AISI 316l stainless steel. *Metall and Mat Trans A*. 2003;34(10):2329-2340.
65. Schwalbe K H. Introduction of δ^5 as an operational definition of the CTOD and its practical applications. *Fracture mechanics: 26th volume*: ASTM; 1997:763-778.
66. Castelluccio GM, McDowell D. Assessment of small fatigue crack growth driving forces in single crystals with and without slip bands. *Int J Fract*. 2012;176(1):49-64.
67. Lim H, Battaile CC, Bishop JE, Foulk JW. Investigating mesh sensitivity and polycrystalline RVEs in crystal plasticity finite element simulations. *Int J Plast*. 2019;121:101-115.
68. Feather WG, Lim H, Knezevic M. A numerical study into element type and mesh resolution for crystal plasticity finite element modeling of explicit grain structures. *Comput Mech*. 2021;67(1):33-55.
69. Holm EA, Battaile CC. The computer simulation of microstructural evolution. *JOM*. 2001;53(9):20-23.
70. Rodgers TM, Madison JD, Tikare V, Maguire MC. Predicting mesoscale microstructural evolution in electron beam welding. *JOM*. 2016;68(5):1419-1426.
71. Manzione PN, Perez-Ipina JE. Plastic hinge model: a generalization to a two-dimensional situation. *Fatigue Fract Eng Mater Struct*. 1994;17(10):1147-1156.
72. Pineau A. Modeling ductile to brittle fracture transition in steels—micromechanical and physical challenges. *Int J Fract*. 2008;150(1):129-156.
73. Castelluccio GM, McDowell DL. Microstructure and mesh sensitivities of mesoscale surrogate driving force measures for transgranular fatigue cracks in polycrystals. *Mater Sci Eng A*. 2015;639:626-639.

How to cite this article: Castelluccio GM, Lim H, Emery JM, Battaile CC. Crack tip microplasticity mediated by microstructure gradients. *Fatigue Fract Eng Mater Struct*. 2021;44:2337–2355. https://doi.org/10.1111/ffe.13493

APPENDIX A

This section presents a mesh sensitivity analysis by considering equiaxed microstructure meshes with same distribution of grains but different number of elements: (a) 1,048, (b) 2,286, (c) 5,341, (d) 9,646, and (e) 21,367 as shown in Figure A1. As mentioned earlier, the previous analysis used meshes with 9,646 elements.

We reconstructed these meshes by the coarsening the mesh (see Castelluccio & McDowell[73]), which results in limited changes in the microstructure due to the loss of grains that are smaller that the element size. Also, we consider the results for ΔCMD and ΔCTD, since we can confidently identify the location of the nodes upon mesh refinement. On the contrary, remeshing can affect the $\Delta\delta_A$ by a changing nodes location ahead of the crack and the eliminating grains upon remeshing. This has not been a problem in previously since all realizations use the same mesh with elements allocated to different grains.

The results shown in Figure A2 demonstrate only some limited mesh sensitivity for ΔCTSD, but the variability shown from refining from 9,646 to 21,367 elements is significantly lower than the microstructural variability shown previously. On the contrary, the results ΔCMOD, ΔCMSD, and ΔCTOD from meshes with 9,646 elements are insensitive to further mesh refinements. Hence, these results demonstrate a limited mesh sensitivity and support the conclusions.

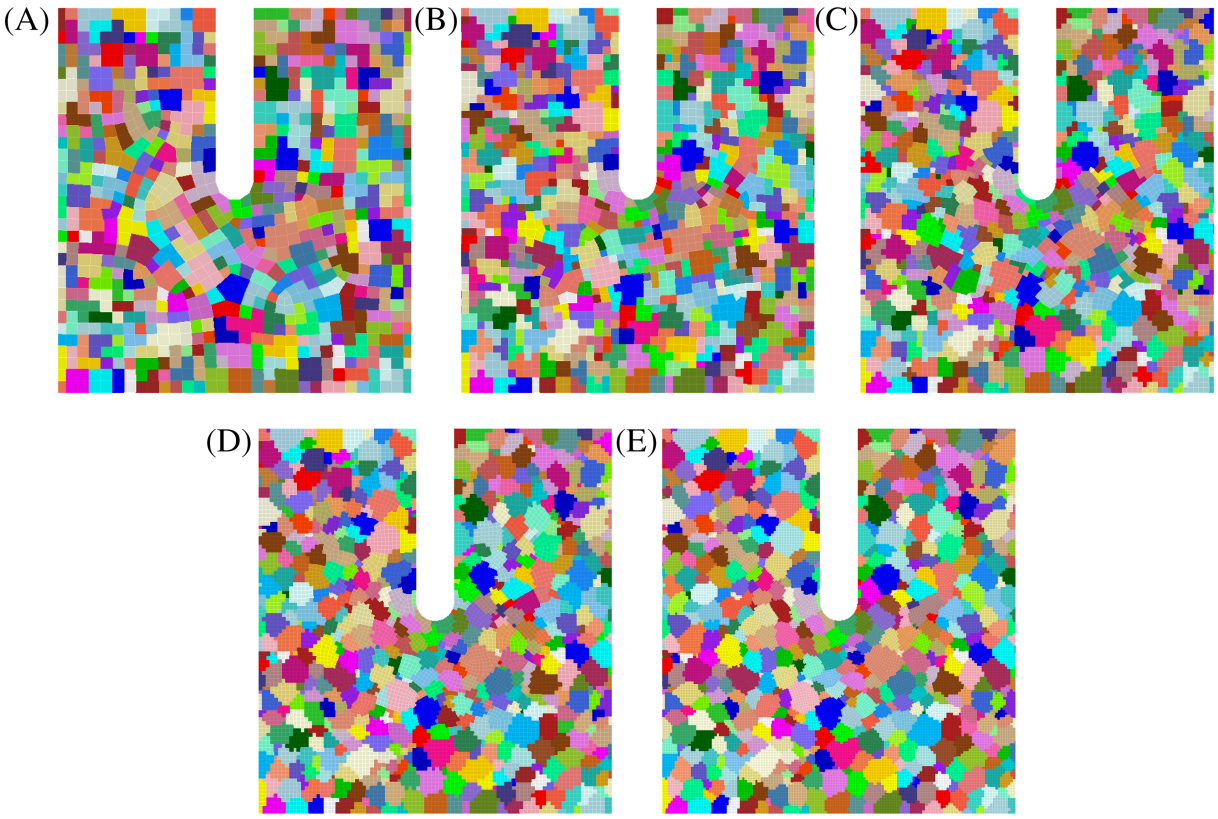


FIGURE A1 Finite element meshes of polycrystalline microstructures with increasing mesh refinement. The models consider the same distribution of grains, but increasing number of elements: (A) 1,048, (B) 2,286, (C) 5,341, (D) 9,646, and (E) 21,367. Colors indicate different grain orientations [Colour figure can be viewed at wileyonlinelibrary.com]

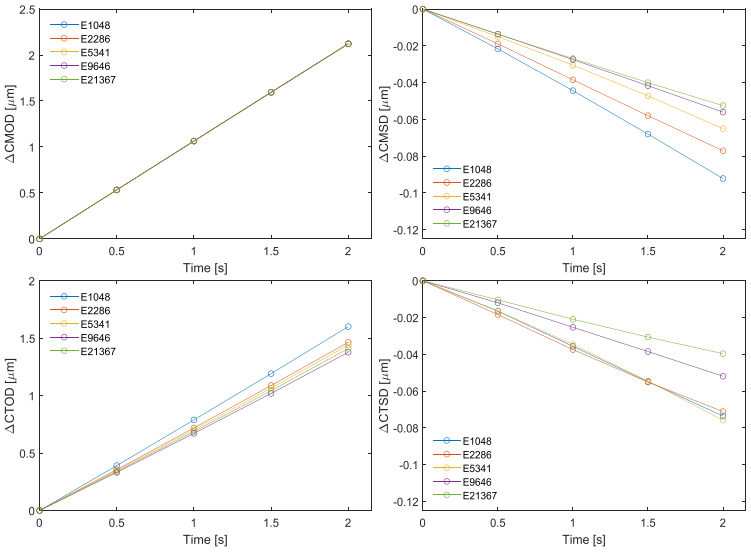


FIGURE A2 Opening (left) and sliding (right) components of the ΔCMD and ΔCTD under displacement control for five meshes with different refinement. The label and color correspond to the number of elements in the simulation [Colour figure can be viewed at wileyonlinelibrary.com]



https://dspace.org/

Crack tip microplasticity mediated by microstructure gradients

Castelluccio, Gustavo M.; Lim, Hojun; Emery, John M.; Battaile, Corbett C.

2021-06-14
Wiley
https://doi.org/10.1111/ffe.13493
Castelluccio GM, Lim H, Emery JM, Battaile C. (2021) Crack tip microplasticity mediated by microstructure gradients. Fatigue and Fracture of Engineering Materials and Structures, Volume 44, Issue 9, September 2021, pp. 2337-2355

Downloaded from a DSpace repository. https://dspace.org/